EAI Endorsed Transactions
on Energy Web

Research Article EAI.EU

Mechanism–Data Dual-Driven Outage Identification Framework for Distribution Networks with High Penetration of Inverter-Based Distributed Generation

Ning Liu[1], Xiaopeng Zhang[1*], Xudong Wang[1,] Guodong Li[2]

[1]State Grid Tianjin Electric Power Company, Tianjin 300010, China
[2]State Grid Tianjin Electric Power Research Institute, Tianjin 300384, China

Abstract

INTRODUCTION: High penetration of inverter-based distributed generators (IBDGs) changes power-flow patterns and fault transients in distribution networks, reducing the effectiveness of conventional outage identification. Under the adopted low-voltage ride-through control model, IBDG fault currents are limited to 1.2–1.5 times the rated current, weakening protection discrimination and degrading classifiers trained on conventional fault features.
OBJECTIVES: To address the aforementioned challenges, this paper proposes a mechanism–data dual-driven outage identification framework for distribution networks with high levels of renewable energy penetration.
METHODS: The framework integrates improved weighted Dempster–Shafer (D–S) evidence theory for multi-source fusion, constructs an IBDG-aware fault-feature library covering converter-specific transient behaviors, and designs decision rules linking post-fault analysis with early fault warning.
RESULTS: Under the tested feeder, DG operating schemes, fault cases, and measurement-noise conditions, the proposed method achieved an F1-score of 96.8%. Its measured model-inference-and-fusion latency was 38 ms, compared with 120 ms for the reference implementation.
CONCLUSION: Under the tested feeder, operating schemes, fault cases, and measurement-noise conditions, the proposed method also achieved higher outage-identification performance than the implemented comparison methods.

Keywords: Active distribution network, distributed generation, outage identification, Dempster–Shafer evidence theory, graph neural network.

Received on 16 August 2026, accepted on 07 September 2026, published on 17 September 2026

doi: 10.4108/ew.14541

1. Introduction

Distributed energy resources (DERs), particularly photovoltaic (PV) and wind generation, are being connected increasingly at the distribution level as decarbonization targets tighten. In several major economies, cumulative distributed-PV capacity has exceeded 300 GW. This expansion reduces emissions and improves local energy autonomy, but it also changes networks designed for radial, unidirectional power delivery [1]. At high DER penetration, feeder power can reverse, renewable output varies over time, and many small converters interact with the upstream grid. These effects violate assumptions used by conventional protection and fault-management schemes [2]. Outage identification must therefore do more than locate a fault after it occurs: it must distinguish genuine faults from DG control responses and recognize abnormal states early enough to

*Corresponding author. Email:569703068@qq.com

support restoration. These functions directly affect interruption duration, self-healing capability, and the resilience of active distribution networks.

Distribution-network fault location remains central to service restoration [3]. In current practice, outage identification relies on customer calls, protection-device status, and a limited set of supervisory control and data acquisition (SCADA) measurements. Because these signals are often processed after an event, restoration can be delayed; smart-meter-based change detection offers a more timely outage-identification path [4]. Advanced metering infrastructure (AMI), distribution-level phasor measurement units (D-PMUs), and intelligent electronic devices (IEDs) provide a denser measurement basis for fault analysis. Recent studies have addressed fault detection, protection, and fault location in distribution networks [5,6]. Spatial–temporal recurrent graph neural networks model the temporal evolution of fault-related measurements while preserving spatial dependencies in the network [7]. Multi-head graph-attention models have been used to learn topology-aware representations for fault location [8]. Domain-adaptive graph models address distribution shifts between training and target operating conditions [9]. Graph-convolutional models have also been applied to fault localization in distribution networks with high DG penetration [10].

Three limitations remain when these methods are applied to distribution networks with high IBDG penetration. First, mechanism-driven methods, including impedance-based fault location and protection coordination, depend strongly on electrical models and protection assumptions. Inverter current limiting and converter control change both the magnitude and waveform of the measured response. Under these conditions, basic probability assignments obtained from conventional analytical models may no longer represent evidence reliability. Fixed D–S combination rules can then amplify rather than resolve conflicts among sources [11].

Second, GCN, temporal recurrent graph, graph-attention, and domain-adaptive graph models can learn fault patterns that are difficult to express analytically. However, their decisions may be difficult to interpret and may deteriorate outside the training distribution. Physics-informed neural networks have been reviewed for power-system applications, where physical constraints are incorporated into the learning process [12]. The original PINN formulation embeds governing equations into the loss function for solving forward and inverse problems [13]. Physics-aware inference has also been proposed for fault location under noisy and incomplete measurements [14]. However, these studies do not specify how learned representations should be reconciled with the mechanism-derived fault evidence used in the present framework.

Restoration-oriented studies have formulated outage management as a joint optimization of repairs, network reconfiguration, and DG dispatch [15]. Other studies have evaluated outage-management performance using resilience metrics for smart-grid applications [16]. Reinforcement-learning methods have also been used for real-time outage management in active distribution networks [17]. These studies primarily address post-outage restoration or operational decision-making rather than the upstream identification of outage states from heterogeneous measurements.

For an inverter-dominated distribution network, outage identification is better formulated as a state-diagnosis problem than as an isolated classification task. The model must relate abnormal measurements to their physical causes, learn the temporal and topological evolution of faults from multiple data sources, and express uncertainty in a form that can support an operating decision. This formulation leads to the mechanism–data dual-driven framework developed in this paper: the physical model constrains interpretation, while the learned model captures patterns that are not represented explicitly by the analytical equations.

In the terminology used here, outage identification denotes the final determination of whether a monitored load section has lost supply; fault diagnosis denotes identification of the underlying fault or abnormal condition; and outage diagnosis denotes the complete procedure that combines event detection, fault analysis, evidence fusion, and decision verification. In this paper, an outage is defined as a loss of supply at one or more distribution transformers or monitored load sections caused by a network fault and the associated protection or switching operation. Scheduled and user-approved maintenance outages are excluded, while communication failures are treated as data-quality events. DG islanding is considered an outage only when the monitored load loses supply; otherwise, it is classified as an islanding state.

The novelty does not lie in the individual use of LSTM, GAT, or D–S theory, but in their explicit integration with an IBDG fault-current and LVRT mechanism model for outage identification under high converter penetration. Mechanism-derived features are converted into evidence and fused with temporal and topology-aware evidence through adaptive reliability weighting. This architecture preserves physical interpretability while maintaining a low-complexity sparse-graph inference path. This combination has not been systematically evaluated for multi-timescale outage identification in IBDG-dominated feeders.

Accordingly, this paper develops a mechanism–data dual-driven outage-identification framework with three contributions:

(1) It establishes a mechanism-to-evidence interface in which IIDG current-limiting and LVRT models generate physically constrained features, while LSTM and GAT modules provide temporal and topology-aware evidence for reliability-dependent D–S fusion.

(2) It formalizes an IBDG-aware feature library containing converter-disconnection, power-surge, LVRT-abnormality, reverse-current, and islanding indicators with defined inputs, thresholds, and outputs. These indicators are converted into basic probability assignments and evaluated through threshold-sensitivity analysis under different DG penetration and noise conditions.

(3) It connects equipment-level risk assessment, area-level propagation analysis, and post-event outage identification. LSTM estimates temporal risk, GAT models topology-dependent spatial influence, and D–S fusion provides an

uncertainty-aware decision. The temporal module is evaluated mainly for early-stage risk assessment; independent long-horizon prediction remains future work.

2. Fault Characteristic Analysis of Distribution Networks with Distributed Generation

Large-scale distributed photovoltaic (DPV) integration changes the fault response on which conventional distribution protection is based. In a passive radial feeder, fault-current direction and magnitude are mainly determined by the upstream source. With inverter-based resources (IBRs), converter controls and local generation influence protection quantities and sequence responses [18], while current-control models determine the magnitude and phase of the inverter contribution [19].

Most modern DPV units use a full-converter interface, maximum power point tracking (MPPT), and a voltage-source converter (VSC). During a fault, the current injected by an inverter-interfaced distributed generator (IIDG) is therefore set mainly by its control and protection loops. This behavior differs from the electromechanical response of a synchronous generator (SG) and must be represented explicitly in the fault model.

2.1 Voltage-Controlled Current Source Characteristics

During a fault, the IIDG is represented as a controlled current source in the synchronous dq reference frame. The d-axis is aligned with the PCC-voltage phasor, and the positive current direction is defined from the IIDG toward the network. The IIDG fault-current phasor and its current limit are formulated as□

$$\begin{gathered}\underline{I}_{\text{fault}}^{\text{IIDG}}(t)=I_d^{\text{ref}}(t)+jI_q^{\text{ref}}(t)\\ I_{\max}^{\text{IIDG}}=\lambda I_N^{\text{IIDG}},\qquad 1.2\le\lambda\le1.5\\ \left|\underline{I}_{\text{fault}}^{\text{IIDG}}(t)\right|=\sqrt{\left[I_d^{\text{ref}}(t)\right]^2+\left[I_q^{\text{ref}}(t)\right]^2}\le I_{\max}^{\text{IIDG}}\end{gathered}\tag{1}$$

where $\underline{I}_{\text{fault}}^{\text{IIDG}}$ is the complex fault-current phasor of the IIDG, I_d^{ref} and I_q^{ref} are the d- and q-axis current references, I_N^{IIDG} is the rated current of the IIDG, $I_{\max}^{\text{IIDG}}$ is its maximum allowable current, and λ is the current-limit factor. The q-axis current reference is determined by the LVRT characteristic in (2), whereas the d-axis current reference is constrained by the remaining converter current capacity in (3). All current quantities in (1)–(3) are expressed using the same RMS or per-unit convention as that adopted in the network simulation. The symbol j is the imaginary unit. This formulation explicitly represents both the control-dependent current direction and the converter current-magnitude limitation.

The adopted mechanism model represents grid-following full-converter PV units under the current-limiting and LVRT control assumptions specified in Section 2. The present formulation does not explicitly model inverter control-mode switching, detailed phase-locked-loop transients, negative-sequence current-control dynamics, or the interaction among heterogeneous PV, battery-energy-storage, and wind-power converters. Therefore, the conclusions concerning IBDG penetration are limited to the control settings and converter types used in the case study.

2.2 Low-Voltage Ride-Through (LVRT) Operation

Low-voltage ride-through (LVRT) requirements keep a DPV unit connected during a voltage dip and require reactive-current support for voltage recovery. In the adopted LVRT control model, the reactive-current reference is determined by the PCC-voltage magnitude as follows:

$$I_q^{ref}=\begin{cases}0, & V_{PCC}>0.9V_N\\ k_1\left(0.9-V_{PCC}/V_N\right)I_N^{\text{IIDG}}, & 0.2V_N\le V_{PCC}\le0.9V_N\\ 1.05\,I_N^{\text{IIDG}}, & V_{PCC}<0.2V_N\end{cases}\tag{2}$$

where I_q^{ref} is the reference reactive current, V_{PCC} is the point of common coupling voltage, V_N is the rated voltage, and k_1 is the reactive current support coefficient. IEEE Std 1547-2018 provides the applicable DER interconnection and abnormal-voltage response requirements [20]; the present study adopts k1 = 2.0. The active current component is correspondingly reduced to comply with the converter current limit:

$$I_d^{ref}=\sqrt{\left(I_{\max}^{\text{IIDG}}\right)^2-\left(I_q^{ref}\right)^2}\tag{3}$$

where $I_{\max}^{\text{IIDG}}$ is the maximum allowable RMS current of the inverter. This voltage-dependent current injection behavior produces complex fault current trajectories that deviate significantly from the exponentially decaying patterns observed in traditional SG-dominated systems.

2.3 Bidirectional Power Flow Characteristics

DPV can also reverse feeder power flow and change the apparent impedance seen by a relay. For a radial feeder with a DPV unit at bus i and a downstream fault at bus j, the DPV contribution to fault current is written as:

$$\dot{I}_{fault}^{DG}=\frac{\dot{E}_{DG}-\dot{V}_{fault}}{Z_{DG}+Z_{line,i-j}}\tag{4}$$

where $\dot{E}_{DG}$ is the equivalent internal voltage of the DPV inverter, Z_{DG} is the equivalent impedance of the inverter filter and coupling transformer, and $Z_{line,i-j}$ is the line impedance between buses i and j. When multiple DPV units are present, the fault current direction becomes ambiguous, potentially leading to protection failure to operate or maloperation.

2.4 Comparative Analysis of Fault Current Levels

To quantify the impact of PV integration on fault current magnitudes, Figure 1 compares the fault current characteristics under different generation scenarios. The non-standard power-factor behavior of inverter controls during faults can further complicate directional discrimination in protection schemes.

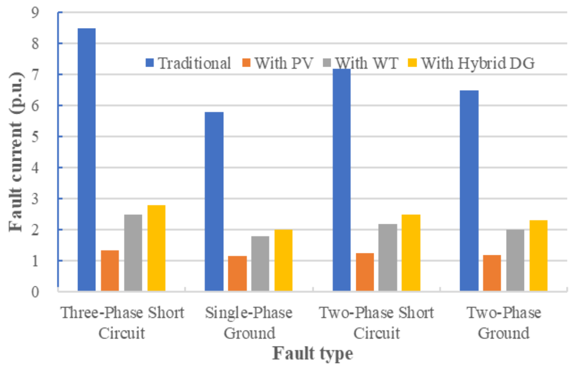

Figure 1. Comparison of fault current characteristics under different generation scenarios

3. Mechanism–Data Dual-Driven Fusion Architecture Design

3.1 Overall Architecture Design

The extensive integration of distributed generators changes the magnitude and direction of fault current and may therefore affect fault diagnosis and the determination of the supply-interruption boundary. Local islanding may leave part of a feeder energized after the upstream grid is interrupted, which makes outage identification more difficult. The proposed architecture combines physical fault-current constraints with temporal, topological, and evidence-fusion information. The validation in this study is limited to network-fault events, the converter settings, the measurement conditions, and the operating schemes described in Sections 2 and 5. Scheduled maintenance outages, communication failures, and weather-induced outages are not quantitatively evaluated. The architecture retains interfaces for future updates using historical outage samples and field measurements.

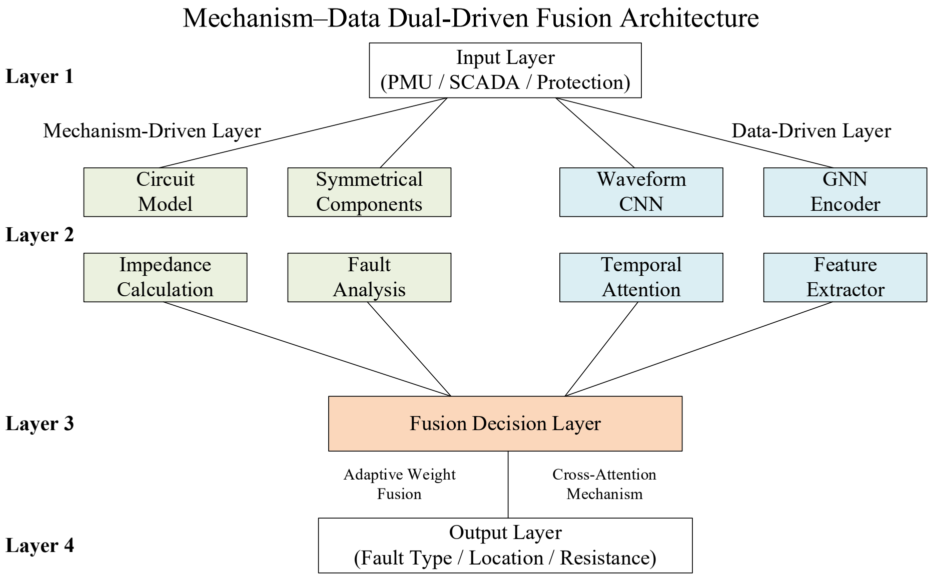

Figure 2. Mechanism–data dual-driven outage-identification architecture for distribution networks

Figure 2 organizes the method into mechanism-driven, data-driven, and fusion-decision layers. The mechanism layer evaluates topology, operating state, and fault-current behavior; the data layer extracts temporal and spatial fault patterns. Each layer maps its result to a basic probability assignment, which gives the fusion layer a common representation for evidence combination. The functions and exchanged quantities are listed in Table 1.

The graph-attention module represents electrical connectivity directly and assigns different message weights to adjacent nodes as a fault propagates. The DG-impact compensation module is used to correct the feature bias caused by the current-limiting and LVRT behavior of inverter-based distributed generators. Its inputs include the measured PCC voltage and current, active and reactive power, IIDG rated current, current-limit factor, LVRT coefficient, and local topology parameters. The expected IIDG current is first calculated using the current-limit and LVRT equations in (1)-(3):

$$\hat{\underline{I}}_{\mathrm{IIDG}}(t) = I_d^{\mathrm{ref}}(t) + jI_q^{\mathrm{ref}}(t) \tag{5}$$

The compensated fault-current feature is then obtained from the measured current and the estimated IIDG contribution:

$$\underline{I}_{\mathrm{res}}(t) = \underline{I}_{\mathrm{meas}}(t) - \hat{\underline{I}}_{\mathrm{IIDG}}(t) \tag{6}$$

The module also generates the current-limit ratio, PCC-voltage deviation, LVRT-state indicator, and reverse-power-flow indicator. These compensated features are passed to the mechanism-driven evidence generator and are not directly used as final fault labels.

Historical sequences help distinguish a short disturbance from a sustained event and reveal gradual equipment degradation. The fusion layer then combines the mechanism-derived evidence with the temporal and spatial evidence generated by the LSTM and GAT modules. This compensation process prevents a fault-current reduction caused by inverter control from being incorrectly interpreted as a remote or high-impedance fault. It therefore improves the physical consistency of the evidence supplied to the subsequent D–S fusion layer.

The parameters of the DG-impact compensation module are the LVRT coefficient k_1=2.0, the PCC-voltage thresholds specified in (2), the current-limit factor λ□ [1.2,1.5], and the IIDG rated current I_N^{IIDG}. The measured and calculated currents use the same RMS or per-unit convention. The compensation module only modifies the diagnostic features and does not change the physical operating state of the IIDG.

Table 1. Functional description of the proposed mechanism–data dual-driven architecture

Layer	Component	Function	Input	Output	Method
Input	Data Acquisition	Multi-source data collection	SCADA, AMI, GIS, meteorological	Preprocessed dataset D	Data cleansing, synchronization
Mechanism-driven	Topology Analysis	Network connectivity verification	D, GIS topology	Adjacency matrix A	Graph theory
Mechanism-driven	Power Flow Calculation	Pre-/post-fault state estimation	A, nodal injections	Voltage profile V, SCR	Newton–Raphson method
Mechanism-driven	Fault Current Calculation	Short-circuit current computation	V, fault location	I_{fault}^{calc}, fault level	Sequence network analysis
Data-driven	GNN Feature Extractor	Spatial correlation learning	A, X	Node embedding $H^{(L)}$	GCN/GAT
Data-driven	LSTM Predictor	Temporal pattern prediction	Time series of X	Fault probability sequence	LSTM
Data-driven	Spectral Clustering	Consumer attribute segmentation	$H^{(L)}$, load profiles	Load cluster labels	Spectral clustering
Fusion	Evidence Fusion	Multi-source belief combination	BPA from mechanism/data layers	Fused diagnosis result	Weighted D–S
Fusion	Decision	Final fault classification	Combined evidence	Fault type and location	Maximum belief rule
Mechanism-driven	DG Impact Compensation	Correct the feature bias caused by IIDG current limiting and LVRT operation	PCC voltage/current, active/reactive power, IIDG rated current, LVRT parameters, and topology parameters	Compensated current residual, current-limit ratio, LVRT-state indicator, and reverse-power-flow indicator	Equations (1)–(3) and residual-based feature correction

3.1.1 Data Input Layer

The data input layer integrates multi-source heterogeneous data from supervisory control and data acquisition (SCADA) systems, advanced metering infrastructure (AMI), geographic information systems (GIS), and meteorological monitoring systems. The preprocessed dataset is expressed as:

$$D = \{(X_t, A, Y_t) \mid t = 1, 2, \ldots, T\} \tag{7}$$

where $X_t \in \mathrm{R}^{N \times d_{feat}}$ is the node feature matrix at time t, $A \in \mathrm{R}^{N \times N}$ is the adjacency matrix representing the network topology, and Y_t is the fault label.

3.1.2 Mechanism-Driven Layer

The mechanism-driven layer employs physics-based models to provide an interpretable analysis of fault events. This layer performs topology analysis to verify network connectivity, conducts power flow calculations to establish pre-fault and post-fault operating states, and executes fault current calculations based on sequence network analysis. The power flow equations for pre-fault steady-state operation are given by:

$$P_i = \sum_{j=1}^{N} |V_i||V_j|\left(G_{ij}\cos\theta_{ij} + B_{ij}\sin\theta_{ij}\right) \tag{8}$$

$$Q_i = \sum_{j=1}^{N} |V_i||V_j|\left(G_{ij}\sin\theta_{ij} - B_{ij}\cos\theta_{ij}\right) \tag{9}$$

where P_i and Q_i are the net active and reactive power injections at bus i, G_{ij} and B_{ij} are the real and imaginary parts of the bus admittance matrix element Y_{ij}, respectively, and $\theta_{ij} = \theta_i - \theta_j$ is the voltage phase angle difference.

For fault current calculation, the positive-sequence, negative-sequence, and zero-sequence networks are constructed and analyzed according to the fault type. The mechanism-driven layer outputs a basic probability assignment (BPA) function $m_M(\cdot)$, representing the belief distribution over fault hypotheses based on physical calculations.

3.1.3 Data-Driven Layer

The temporal module is based on the long short-term memory (LSTM) architecture [21]. For spatial feature extraction, the network is represented as a graph and processed using graph convolutional networks (GCNs) [22] or graph attention networks (GATs) [23]. In the present implementation, the GAT branch is used as the primary spatial module, while the GCN is used as the ablation baseline:

$$H^{(l+1)} = \sigma\left(\tilde{D}^{-1/2}\tilde{A}\tilde{D}^{-1/2}H^{(l)}W^{(l)}\right) \tag{10}$$

where $\tilde{A} = A + I_N$ is the adjacency matrix with self-loops, $\tilde{D}_{ii} = \sum_j \tilde{A}_{ij}$ is the degree matrix, $W^{(l)}$ is the learnable weight matrix of layer l, $\sigma(\cdot)$ is the activation function, and $H^{(l)}$ is the node embedding at layer l with $H^{(0)} = X$.

Temporal pattern prediction utilizes long short-term memory (LSTM) networks to model the sequential evolution of fault features:

$$c_t = f_t \odot c_{t-1} + i_t \odot \tanh\left(W_c\left[h_{t-1}, x_t\right] + b_c\right) \tag{11}$$

$$h_t = o_t \odot \tanh\left(c_t\right) \tag{12}$$

where i_t, f_t, and o_t are the input, forget, and output gates, respectively, c_t is the cell state, and h_t is the hidden state at time t.

The data-driven layer outputs a BPA function $m_D(\cdot)$ derived from the softmax probabilities of the trained neural network classifier.

3.1.4 Fusion Decision Layer Based on Improved Weighted D–S Evidential Theory

The fusion decision layer employs an improved weighted D–S evidential theory to combine the BPA outputs from the mechanism-driven and data-driven layers. The traditional D–S combination rule may produce counterintuitive results under conditions of strong evidence conflict [24]. To address this issue, an adaptive weighting mechanism based on the credibility and reliability of each evidence source is introduced.

Let $\Theta = \{F_1, F_2, \ldots, F_K\}$ denote the frame of discernment comprising K possible fault types. The weighted BPA functions are defined as:

$$m'_i(A) = w_i \cdot m_i(A), \quad \forall A \subseteq \Theta, A \neq \Theta \tag{13}$$

$$m'_i(\Theta) = 1 - w_i \cdot \sum_{B \subset \Theta} m_i(B) \tag{14}$$

where $w_i \in [0,1]$ is the adaptive weight of the evidence source i. The weights are computed based on the information entropy of the evidence source:

$$\bar{H}_i = \frac{H_i}{\log|\Theta|}$$

$$w_i = \frac{r_i \exp(-\alpha \bar{H}_i)}{\sum_{j=1}^{S} r_j \exp(-\alpha \bar{H}_j)}, \quad r_i \in [r_{\min}, 1] \tag{15}$$

$$\sum_{i=1}^{S} w_i = 1$$

$$H_i = -\sum_{A \subseteq \Theta} m_i(A) \log_2 m_i(A) \tag{16}$$

where H_i is the Shannon entropy of the i-th evidence source, S is the total number of evidence sources, and α is a temperature hyperparameter controlling the sensitivity to entropy variation. A lower entropy (more concentrated belief distribution) receives a higher weight, reflecting greater confidence in that evidence source. $\bar{H}_i$ is its normalized entropy, and r_i is a validation-based reliability coefficient. Entropy measures the concentration of a belief distribution but does not directly measure its correctness. Therefore, the entropy term is combined with r_i, which is estimated from a class-balanced validation set using a calibration or Brier-score criterion. The clipping operation guarantees $r_i \in [r_{\min}, 1]$, while the normalization in (13) guarantees $w_i \in [0,1]$ and $\sum_{i=1}^{S} w_i = 1$. The combined BPA using Dempster's rule of combination is:

$$m(A) = \frac{1}{1 - K_c} \sum_{A_1 \cap A_2 = A} m'_1(A_1) m'_2(A_2) \tag{17}$$

where K_c is the conflict coefficient. The conflict threshold K_{th} is selected from the validation set rather than assigned arbitrarily. Let $T \subset [0,1]$ be a candidate threshold set. The selected threshold is determined by

$$K_{\text{th}} = \arg\max_{\tau \in T} \text{MacroF1}_{\text{val}}(\tau) \tag{18}$$

subject to

$$\text{FAR}_{\text{val}}(\tau) \leq \delta \tag{19}$$

where δ is the maximum allowable false-alarm rate specified by the operational requirement. Dempster's combination rule is used when $K_c \leq K_{\text{th}}$, whereas Yager's combination rule is applied when $K_c > K_{\text{th}}$, as follows:

$$m_Y(A) = \sum_{A_1 \cap A_2 = A} m'_1(A_1) m'_2(A_2), \quad A \neq \varnothing, A \neq \Theta \tag{20}$$

$$m_Y(\Theta) = 1 - \sum_{B \subset \Theta} m_Y(B) \tag{21}$$

The final diagnosis decision is made by selecting the hypothesis with the maximum belief:

$$F^* = \arg\max_{F_k \in \Theta} m(F_k) \tag{22}$$

subject to $m(F^*) > \beta_{th}$, where β_{th} is a decision threshold ensuring sufficient confidence in the diagnosis result.

3.2 Fault Feature-Based Diagnosis Rule Design

Conventional diagnosis uses relay-operation records, breaker-state changes, and voltage or current limit violations as its main criteria. These signals are less definitive in a DPV-rich feeder. Converter current limiting may keep the measured current below a protection pickup value; DPV disconnection can produce a voltage excursion that resembles a network fault; and an energized island must be distinguished from an actual loss of supply. The diagnosis rules must therefore include converter and islanding behavior in addition to conventional protection signals.

Three DPV-specific triggers are added to address these ambiguities: renewable-energy disconnection, rapid power change, and abnormal LVRT response. They supplement rather than replace the conventional criteria.

3.2.1 Renewable Energy Disconnection Triggering Condition

A DPV unit may disconnect after detecting a fault or another abnormal condition. The resulting step in active power, together with the accompanying PCC-voltage deviation, is used to distinguish a disconnection event from ordinary output variation. The trigger is defined as:

$$T_{trip}^{DG} = \begin{cases} 1, & \text{if} \Delta P_{DG} > \eta_P \cdot P_N^{DG} \text{and} \Delta V_{PCC} > \eta_V \cdot V_N \\ 0, & \text{otherwise} \end{cases} \tag{23}$$

where $\Delta P_{DG} = \left| P_{DG}(t) - P_{DG}(t-\Delta t) \right|$ is the active power variation of the DPV unit, η_P is the active power variation threshold coefficient (typical value $\eta_P = 0.8$), η_V is the voltage deviation threshold coefficient (typical value $\eta_V = 0.05$), and Δt is the detection time window (typical value $\Delta t = 100$ ms).

3.2.2 Power Surge Triggering Condition

Rapid power fluctuations caused by DPV disconnection or LVRT mode switching can serve as auxiliary fault indicators. The power surge triggering formula is:

$$T_{surge}^{P} = \begin{cases} 1, & \text{if} \left| \frac{dP}{dt} \right| > \lambda_P \text{or} \left| \frac{dQ}{dt} \right| > \lambda_Q \\ 0, & \text{otherwise} \end{cases} \tag{24}$$

where λ_P and λ_Q are the active and reactive power rate-of-change thresholds, respectively. The derivatives are approximated using finite differences over a sliding window:

$$\frac{dP}{dt} \approx \frac{P(t_k) - P(t_{k-W})}{t_k - t_{k-W}} \tag{25}$$

where W is the sliding window size. Typical threshold values are $\lambda_P = 0.3 P_N$ / s and $\lambda_Q = 0.2 Q_N$ / s for distribution lines with moderate DPV penetration.

3.2.3 LVRT Abnormality Triggering Condition

Abnormal behavior during the LVRT process may indicate either a real grid fault or a DPV control failure. The LVRT abnormality triggering condition monitors the consistency between the measured reactive current injection and the grid code requirements:

$$T_{LVRT}^{abn} = \begin{cases} 1, & \text{if} \left| I_q^{actual} - I_q^{ref}(V_{PCC}) \right| > \grave{o}_q \text{and} \delta_{LVRT} = 1 \\ 0, & \text{otherwise} \end{cases} \tag{26}$$

where I_q^{actual} is the measured reactive current, $I_q^{ref}(V_{PCC})$ is the reference value required by the grid code (as defined in (2)), $\grave{o}_q$ is the tolerance threshold (typical value $\grave{o}_q = 0.1 I_N^{DG}$), and $\delta_{LVRT} = 1$ indicates active LVRT mode operation.

3.2.4 Composite Triggering Logic

The overall diagnosis trigger combines the conventional criteria with the three new conditions through a weighted OR logic:

$$T_{total} = w_{trad} \cdot T_{trad} + w_{trip} \cdot T_{trip}^{DG} + w_{surge} \cdot T_{surge}^{P} + w_{LVRT} \cdot T_{LVRT}^{abn} \tag{27}$$

where T_{trad} represents the combined conventional triggers (protective relays, circuit breakers, limit violations), and the weights satisfy $w_{trad} + w_{trip} + w_{surge} + w_{LVRT} = 1$. The fault diagnosis procedure is initiated when $T_{total} > T_{th}$, where T_{th} is a global triggering threshold.

4. Outage Identification Procedure for Distribution Networks with Distributed Generation

The outage-identification method contains three connected modules. The LSTM module uses electrical, environmental, and equipment-state histories to estimate when fault risk is increasing. The graph model combines feeder topology with nodal measurements to locate the likely affected area. These temporal and spatial outputs are converted to evidence and combined by the improved weighted D–S rule, which represents source conflict and epistemic uncertainty explicitly. Thus, the first two modules answer different parts of the diagnosis problem—time and location—while the third determines whether their evidence is sufficiently consistent for a decision. Rule-based triggers subsequently initiate data acquisition, fusion, verification, and notification, forming the closed diagnostic loop.

4.1 Fault Probability Prediction Based on Historical Data Mining

4.1.1 LSTM-Based Temporal Fault Probability Modeling

The LSTM network processes sequential input features $\boldsymbol{x}_t = \left[x_t^{(1)}, x_t^{(2)}, \ldots, x_t^{(d)}\right] \in \mathbb{R}^d$ at each time step t, where the input feature dimension d encompasses three categories of monitoring variables:

- Electrical quantities: nodal voltage magnitude V_i, branch current phasor I_{ij}, active/reactive power flow P_{ij}, Q_{ij}, and power quality indices (THD, voltage unbalance factor);
- Environmental quantities: ambient temperature T_a, relative humidity H_r, rainfall intensity R_p, wind speed W_s, and lightning stroke density ρ_L;
- Equipment state quantities: equipment age τ_{eq}, cumulative operating time t_{op}, maintenance cycle index γ_m, historical fault count n_f, and thermal overload ratio η_{th}.

The LSTM cell state update equations are given by:

$$\begin{aligned}
f_t &= \sigma\left(W_f \cdot [h_{t-1}, x_t] + b_f\right) \\
i_t &= \sigma\left(W_i \cdot [h_{t-1}, x_t] + b_i\right) \\
\tilde{C}_t &= \tanh\left(W_C \cdot [h_{t-1}, x_t] + b_C\right) \\
C_t &= f_t \odot C_{t-1} + i_t \odot \tilde{C}_t \\
o_t &= \sigma\left(W_o \cdot [h_{t-1}, x_t] + b_o\right) \\
h_t &= o_t \odot \tanh\left(C_t\right)
\end{aligned} \tag{28}$$

The fault probability output is computed through a fully connected regression layer:

$$\hat{p}_f(t) = \mathrm{sigmoid}\left(W_{fc} \cdot h_T + b_{fc}\right) \in [0,1] \tag{29}$$

The model is trained using a binary cross-entropy loss with L2 regularization:

$$\mathcal{L}_{LSTM} = -\frac{1}{N}\sum_{n=1}^{N}\left[y_n \log\left(\hat{p}_{f,n}\right) + (1-y_n)\log\left(1-\hat{p}_{f,n}\right)\right] + \lambda\|\Theta\|_2^2 \tag{30}$$

The LSTM gates mitigate vanishing gradients and retain dependencies over tens or hundreds of monitoring intervals. This is relevant to precursors that develop gradually and then change abruptly, such as insulation deterioration, line icing, and transformer-oil temperature. The input variables represent three distinct sources of information: currents and voltages describe the electrical operating state; temperature, humidity, and wind speed describe accumulated environmental stress; and switching counts or protection alarms indicate equipment condition. These variables are consistent with the monitoring and condition-assessment data used in modern asset-management practice [25].

The LSTM is trained to regress fault probability rather than output only a fault label. A discrete classifier would provide one decision at each interval, whereas the probability sequence preserves how risk evolves in time. That sequence can also be mapped directly to a continuous basic probability assignment for the subsequent D–S fusion, retaining information that would be lost after hard classification.

4.1.2 GNN-Based Fault Location Prediction

The framework models the distribution network as an undirected graph $G = (V, E, A)$, and employs a Graph Attention Network (GAT) to learn discriminative node representations. The attention mechanism computes importance coefficients between connected nodes:

$$e_{ij} = \mathrm{LeakyReLU}\left(a^T \cdot \left[Wh_i \| Wh_j\right]\right) \tag{31}$$

$$\alpha_{ij} = \frac{\exp\left(e_{ij}\right)}{\sum_{k \in \mathcal{N}(i)} \exp\left(e_{ik}\right)} \tag{32}$$

$$h'_i = \sigma\left(\sum_{j \in \mathcal{N}(i)} \alpha_{ij} W h_j\right) \tag{33}$$

A multi-head attention mechanism is adopted:

$$h'_i = \Big\|_{k=1}^{K} \sigma\left(\sum_{j \in \mathcal{N}(i)} \alpha_{ij}^{(k)} W^{(k)} h_j\right) \tag{34}$$

The LSTM–GAT structure is adopted as an engineering design choice rather than as a claim that either LSTM or GAT is individually novel. The LSTM module models the temporal evolution of electrical and equipment-state measurements, whereas the GAT module extracts topology-dependent spatial features from the distribution network. In a radial distribution network, fault influence is not uniformly distributed across neighboring nodes but depends on electrical distance, line impedance, power-flow direction, and DG operating conditions. The attention coefficients of GAT can therefore learn the relative influence between connected nodes and provide an interpretable representation of topology–electrical coupling.

Compared with spatial–temporal graph convolutional networks (STGCNs), which usually combine predefined graph convolutions with temporal convolution blocks, the proposed separated LSTM–GAT structure preserves the temporal and spatial evidence as two distinguishable features before the subsequent D–S fusion. This separation is useful because the temporal evolution of an equipment signal and the spatial propagation of a fault may have different reliability levels under noisy measurements. Compared with graph Transformer models, which employ global node-to-node attention and can capture long-range dependencies, GAT uses sparse neighborhood attention that is more consistent with the local connectivity of a radial feeder and has lower attention complexity for the network size considered in this study. The multi-head GAT further allows different propagation patterns, such as line faults, DG islanding, and load transfer, to be represented in parallel.

Therefore, the LSTM–GAT structure is selected because it provides a suitable balance among temporal modeling, topology-aware spatial representation, interpretability, and computational cost for the studied distribution network. This comparison describes the design rationale of the proposed architecture and should not be interpreted as an empirical claim that LSTM–GAT is universally superior to STGCN or graph Transformer models, since those models are not included as independent baselines in the present experiment.

4.1.3 Three-Level Progressive Prediction System

The three-level progressive prediction system mirrors the hierarchy of fault evolution from individual equipment to affected areas and, ultimately, the entire distribution system. At the equipment level, the LSTM analyzes the historical monitoring sequence of each component and estimates its probability of developing a fault or abnormal condition. These equipment-level probabilities are then used as prior evidence for the area-level GAT. By combining the estimated equipment risks with feeder topology and power-flow coupling, the GAT captures the spatial influence among neighboring components and calculates a risk index for the corresponding feeder or substation area. At the system level, the outputs from all areas are further aggregated with DG-penetration factors and topology-centrality factors to obtain a network-wide vulnerability score. This hierarchical process progressively narrows the diagnostic search from high-risk equipment to potentially affected areas and finally to the whole network, while providing interpretable intermediate results for operator review. It also supports different decision horizons: equipment-level screening enables rapid event detection, area-level assessment assists dispatch and fault-isolation decisions, and system-level assessment supports operational planning. The practical implementation of this hierarchical process is illustrated below using a typical branch-line outage event, together with its associated data sources and event-screening criteria.

To illustrate the hierarchical process, a typical branch-line outage is defined as a line fault that does not de-energize the entire main line but simultaneously interrupts two or more distribution transformers. The event structure is shown in Figure 3. The distribution automation system provides fault-indicator alarms, sectioning- and branch-switch state changes, branch load data, protection-action records, and transformer outage/restoration events. The electricity information collection system provides synchronized outage/restoration records and operating load parameters for public and special transformers. Repeated switch-trip and transformer-outage signals within the same event window are merged. Planned outages, user-approved outages, and voluntary shutdowns are removed using marketing-system tags. Switching records for which the pre-action current is less than 0.003 times the rated current are treated as debugging signals and discarded.

After preprocessing, a branch-line outage event is retained only when four checks are satisfied: signal validity, time validity, branch-line outage characteristics, and transformer-load consistency. An outage shorter than 3 min, or a restoration signal without a preceding outage record within the previous 24 h, is rejected. The system then checks for an effective opening of a sectioning or branch switch or a short-circuit alarm from a nearby fault indicator. If no switch-state change is available, synchronous outage reports from at least two transformers on the same feeder within the allowable clock-deviation range are sufficient to identify a branch-line outage. Finally, two outage transformers are randomly selected for phase-A voltage inspection; a zero, blank, or nonresponsive voltage reading provides an independent consistency check. The resulting event definition is used in Figure 3.

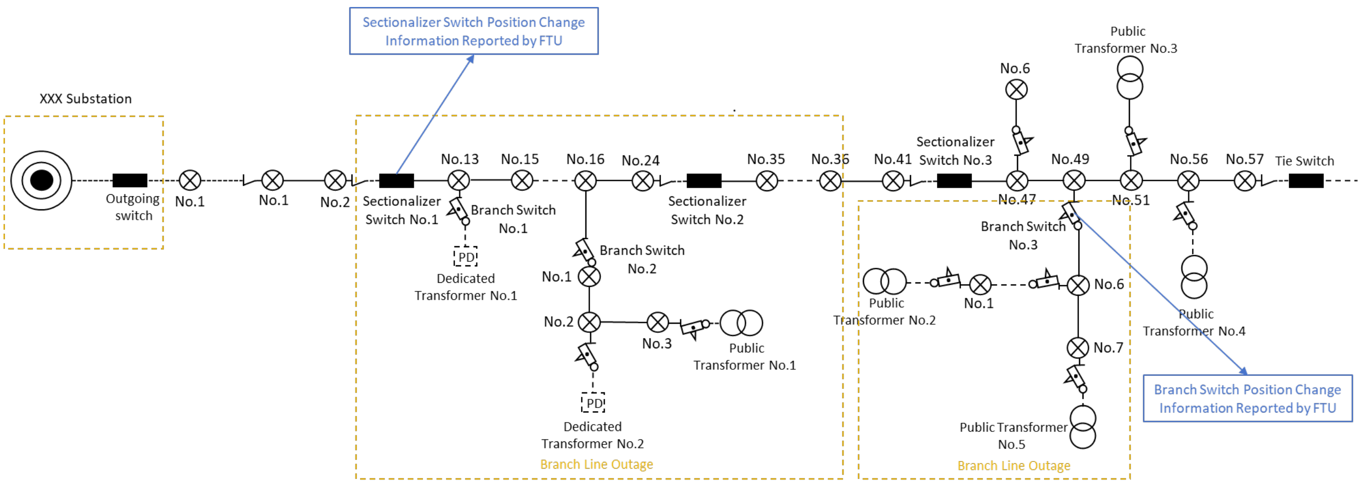

Figure 3. Typical structure for identifying branch-line outage events

4.2 Data-Driven Module for Outage Identification

Trigger priorities are assigned according to the expected propagation timescale of each event. P1 is reserved for protective-relay operation and voltage-collapse events. DG disconnection and islanding-related triggers are assigned to P2 in accordance with Table 2. From P2 to P5, the allowable response times are progressively relaxed as the associated abnormal conditions evolve more slowly. This priority structure allocates computational and communication resources according to event urgency while avoiding unnecessary processing for slower-changing conditions. The trigger set includes conventional criteria, such as relay operation, abnormal voltage deviations, and protection-status changes, as well as DG-specific criteria, including islanding detection and LVRT failure. The latter criteria are necessary because bidirectional power flow and converter-controlled operation cannot be fully characterized by traditional protection signals alone. Therefore, the P1–P5 structure provides a timescale-based decomposition of the fault evolution process and determines which diagnostic routine should be activated at each stage.

Algorithm 1: Intelligent Outage Diagnosis and Assessment

Input: Distribution network graph G; real-time measurement stream $M(t)$; historical database D_h; trigger condition set T; confidence threshold η_{th}; maximum iteration count κ_{max}

Output: outage-identification decision $F^* = \{f_{type}, f_{location}, f_{probability}, \tau_{confidence}\}$

Procedure:

1. Initialize pre-trained LSTM model M_{LSTM}, GAT model M_{GAT}, and fusion parameters.
2. **Trigger Monitoring**: Continuously monitor $M(t)$ for matches with trigger set T.
3. **Priority Scheduling**: Dequeue the highest-priority trigger τ^* from priority queue Q.
4. **Data Acquisition**: Collect multi-source data within window $[t_{detect} - \Delta t, t_{detect}]$ for the affected area.
5. **Preprocessing**: Perform bad data detection, denoising, and normalization.
6. **Three-Level Prediction**: Compute equipment-level probability via LSTM, regional risk index via GAT, and determine candidate fault location set L_{cand}.
7. **Dual-Drive Analysis**: Generate temporal evidence E_1 (BPA m_1 from LSTM), spatial evidence E_2 (BPA m_2 from GAT), protection evidence E_3 (BPA m_3), and electrical evidence E_4 (BPA m_4).
8. **Improved D–S Fusion**: Compute reliability weights and iteratively fuse evidence.
9. **Decision Verification**: Output final decision if $\tau_{confidence} \geq \eta_{th}$; otherwise request supplementary evidence.
10. **Logging and Notification**: Record results and send control signals.

Computational Complexity Analysis:

Let N and E denote the numbers of graph nodes and edges, T the temporal-window length, M the number of measurement channels, L_G and L_L the numbers of GAT and LSTM layers, H the number of attention heads, d_l the feature width of GAT layer l, h_l the hidden dimension of LSTM layer l, S the number of evidence sources, K the number of fault hypotheses, and R the maximum number of evidence-fusion iterations. The computational cost of one diagnosis instance is bounded by

$$C_{\text{total}} = O\Big(TM + \sum_{l=0}^{L_G-1}\big(Nd_l d_{l+1} + HEd_{l+1}\big) + T\sum_{l=1}^{L_L} 4h_l\big(h_{l-1} + h_l + 1\big) + I_{\text{pf}} C_{\text{pf}}(N,E) + RS^2K^2\Big) \tag{35}$$

where $C_{\text{pf}}(N,E)$ is the computational cost of the selected power-flow or fault-current solver and I_{pf} is its iteration count. The corresponding memory requirement is $O\big(TM + \sum_l Nd_l + \sum_l h_l + SK\big)$.

This formulation explicitly describes the dependence of the proposed method on network size, temporal-window length, feature dimensions, graph connectivity, and evidence-fusion iterations. For the IEEE 33-bus case used in this study, the variables in this expression should be substituted with the actual model dimensions and solver settings.

Let $\Theta = \{\theta_1, \theta_2, \ldots, \theta_M\}$ denote the frame of discernment comprising six primary fault hypotheses: single line-to-ground (LG), line-to-line short circuit (LL), double line-to-ground (LLG), three-phase short circuit (LLL), three-phase-to-ground (LLLG), and high impedance fault (HIF), plus an uncertainty hypothesis $\theta_7 = \Theta$. The reliability weight for each evidence source is defined as:

$$w_i = \alpha \cdot SCR_i + \beta \cdot (1 - \mathrm{Var}_i) + \gamma \cdot R_i^2 \tag{36}$$

where α, β, and γ are hyperparameters with empirical values of 0.4, 0.35, and 0.25, respectively.

The weighted basic probability assignment (BPA) is given by $\tilde{m}_i(A) = w_i \cdot m_i(A),\ \forall A \subseteq \Theta$.

The combined BPA using Dempster's rule is:

$$m(A) = \frac{1}{1-K} \sum_{A_i \cap B_j = A} \tilde{m}_1(A_i) \cdot \tilde{m}_2(B_j) \tag{37}$$

Table 2 summarizes the trigger conditions and priority classification for the diagnosis rules. When $\max_A m(A) < \eta_{th}$ (with $\eta_{th} = 0.65$), the system activates the supplementary evidence request mechanism, triggering additional data acquisition from high-resolution sensors or adjacent monitoring nodes. This process iterates until the confidence threshold is satisfied or the maximum iteration count $\kappa_{max} = 3$ is reached.

Table 2. Trigger Conditions and priority classification for diagnosis rules

Priority	Category	Trigger Condition	Response Time Limit	Threshold
P1 (Critical)	Protective relay operation	Relay tripping signal detected	≤ 20 ms	Any relay status change
P1 (Critical)	Voltage collapse	Bus voltage $V <$ 0.7 p.u.	≤ 20 ms	V_{min} = 0.7 p.u.
P2 (High)	Frequency deviation	$\lvert f - f_0 \rvert >$ 0.5 Hz	≤ 50 ms	—
P2 (High)	DG disconnection event	DG inverter islanding detected	≤ 50 ms	LVRT violation
P2 (High)	Abnormal fault current	$\lvert I_{fault} \rvert >$ 1.5 × I_{pickup}	≤ 50 ms	—
P3 (Medium)	LSTM probability warning	$\hat{p}_f >$ 0.7	≤ 100 ms	η_p = 0.7
P3 (Medium)	Power quality violation	THD > 8% or VUF > 3%	≤ 100 ms	IEEE 519 limits
P3 (Medium)	Communication failure	SCADA data timeout	≤ 100 ms	$t_{timeout}$ = 5 s
P4 (Low)	Load imbalance anomaly	Phase current unbalance > 20%	≤ 200 ms	δ_{imb} = 0.20
P4 (Low)	Thermal overload	Equipment temperature exceeds rated value	≤ 200 ms	Nameplate rated temperature
P5 (Planned)	Maintenance window	Scheduled inspection period	≤ 500 ms	Calendar trigger
P5 (Planned)	Weather warning	Severe weather alert	≤ 500 ms	Meteorological warning

5. Case Study and Verification

5.1 Test System Description

The test system is a practical urban radial distribution area in China with a total demand of 3.715 MW and 2.300 Mvar. Five buses are available for DG installation. Table 3 defines four operating schemes: Scheme A contains no DG and retains unidirectional feeder flow, whereas Schemes B, C, and D increase DG penetration to 15%, 30%, and 45%, respectively. These three values are used in this study to represent low-, medium-, and high-penetration conditions. The sequence provides a common network on which the diagnostic method can be tested as the feeder changes from a passive load network to an active distribution network.

In this study, DG penetration is defined as the ratio of the total installed active-power capacity of the IBDG units to the total peak active load of the studied feeder:

$$\eta_{\mathrm{DG}} = \frac{P_{\mathrm{DG,cap}}}{P_{\mathrm{load,peak}}} \times 100\% \tag{38}$$

It represents capacity penetration rather than the actual energy-generation share. With $P_{\mathrm{load,peak}}$ =3.715 MW, the DG capacities of 0.557, 1.115, and 1.672 MW correspond to approximately 15%, 30%, and 45%, respectively.

Table 3. DG Configuration schemes for fault feature analysis

Parameter	Scheme A (No DG)	Scheme B (Low Penetration)	Scheme C (Medium Penetration)	Scheme D (High Penetration)
DG Capacity Penetration (%)	0%	15%	30%	45%
DG Total Capacity (MW)	0	0.557	1.115	1.672
DG Installation Number	0	2	3	5
DG Locations (Bus)	—	13, 25	6, 13, 25	6, 13, 18, 25, 30
DG Type	—	Inverter-based	Inverter-based	Inverter-based
Control Mode	—	PQ/VF Droop	PQ/VF Droop	PQ/VF Droop
Short Circuit Ratio (SCR)	—	5.2	3.8	2.6

Table 4 shows how the fault signature changes across the four schemes. The ratio of maximum to minimum fault current falls from 6.09 to 2.55, so the amplitude separation used by overcurrent protection becomes smaller and the coordination margin is reduced. At the same time, the voltage-unbalance factor rises from 0% to 13.24%, indicating that criteria based on symmetrical components become more sensitive to the operating point and phase imbalance. The probability of protection failure to operate increases from 0% to 24.6%. This trend is consistent with the mechanism discussed in Section II: DG alters the current seen by the upstream relay and can leave it below the pickup setting for a downstream fault. The DG contribution ratio reaches 44.8%, and 34 reverse-current events are recorded in Scheme D, confirming that the current distribution is no longer governed by the upstream source alone.

Table 4. Fault characteristic parameters under different dg penetration scenarios

Parameter	Scheme A (0%)	Scheme B (15%)	Scheme C (30%)	Scheme D (45%)	Trend
Maximum Fault Current (p.u.)	6.82	6.45	5.91	5.23	Decreasing
Minimum Fault Current (p.u.)	1.12	1.38	1.67	2.05	Increasing
Fault Current Range Ratio	6.09	4.67	3.54	2.55	Decreasing
Maximum Voltage Dip Depth (%)	82.3	76.5	68.2	59.7	Decreasing
Voltage Unbalance Factor (%)	0.00	3.42	7.86	13.24	Increasing
DG Contribution Ratio (%)	0.00	18.5	32.7	44.8	Increasing
Reverse Current Event Count	0	8	19	34	Increasing
Protection Failure Probability (%)	0.00	5.2	12.8	24.6	Increasing
Fault Location Error (%)	8.5	12.3	18.7	27.4	Increasing
Total Harmonic Distortion THD (%)	2.1	4.8	8.3	13.6	Increasing
Symmetrical Component Ratio I2/I1	0.58	0.52	0.45	0.38	Decreasing

To further visualize the influence of DG penetration on fault-current dynamics, Figure 4 presents the fault current waveforms under different DG penetration scenarios. As DG penetration increases from 0% to 45%, the peak fault current gradually decreases, and the post-fault current response becomes less pronounced. This phenomenon is mainly caused by the current-limiting control and low-voltage ride-through behavior of inverter-based DGs, which weaken the fault-current contribution and reduce the distinguishability of traditional overcurrent-based protection criteria.

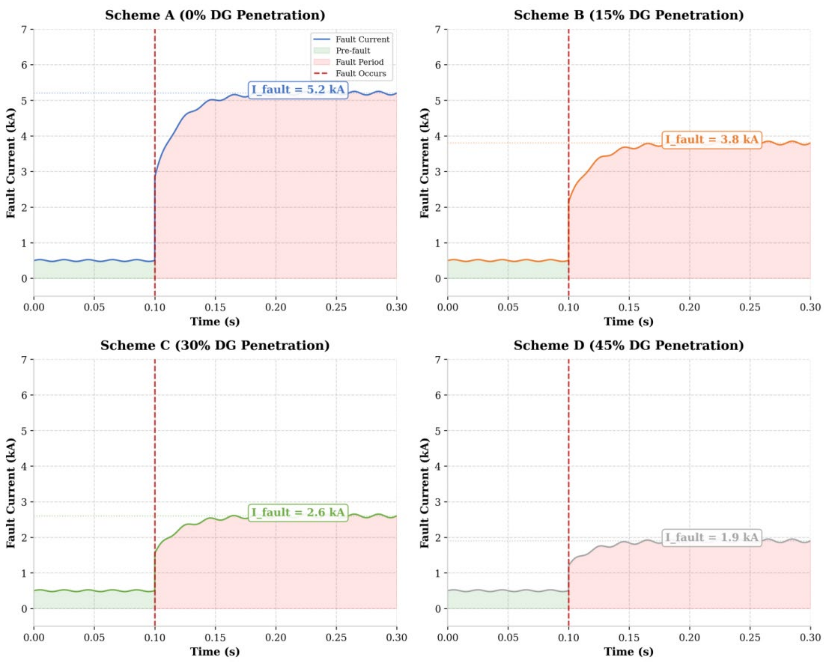

Figure 4. Fault current waveforms under different DG penetration scenarios.

5.2 Outage-Identification Performance Comparison and Verification

For a reproducible comparison, three baseline methods are defined. The traditional topology-based method (TTM) uses the known radial topology, sequence-network fault-current calculation, relay pickup logic, and switch-state information to identify the faulted section. The matrix-analysis method (MA) formulates fault localization using network equations and voltage-current residuals. Its parameters are obtained from the nominal network model. The pure graph-learning method (PG) applies a graph convolutional or graph-attention model directly to the network topology and nodal measurements and performs an end-to-end diagnosis. All three baselines use the same test events, measurement windows, sampling conditions, preprocessing procedure, and evaluation metrics as the proposed method. Baseline parameters and thresholds are determined using the training or validation data only.

To quantify the robustness of each method against measurement noise, the anti-noise score S_{AN} is defined as the relative retention of the F1-score under noisy measurements:

$$S_{\mathrm{AN}} = 100 \times \frac{\frac{1}{|\mathrm{S}|}\sum_{s\in \mathrm{S}} F1(s)}{F1(40\ \mathrm{dB})} \tag{39}$$

where S={35,30,25,20,15,10} dB and $F1(s)$ denotes the F1-score obtained at SNR s. The 40 dB result is used as the reference performance. A higher S_{AN} indicates better retention of diagnostic performance as the measurement noise increases.

An end-to-end deployment latency can be conceptually decomposed as

$$\begin{aligned} T_{\mathrm{total}} &= T_{\mathrm{acq}} + T_{\mathrm{comm}} + T_{\mathrm{sync}} + T_{\mathrm{pre}} + T_{\mathrm{mech}} \\ &+ T_{\mathrm{LSTM}} + T_{\mathrm{GAT}} + T_{\mathrm{fusion}} + T_{\mathrm{decision}} \end{aligned} \tag{40}$$

In the present study, only the model-inference-and-fusion stage was timed. The reported 38 ms therefore denotes a measured model-side latency rather than the complete end-to-end latency T_{total}. Data acquisition, inter-device communication, timestamp synchronization, and field-device actuation were not included or separately measured. The 38 ms result should therefore be interpreted as a case-study inference-and-fusion measurement rather than a device-independent real-time deployment result.

Figure 5 presents an aggregate comparison of the proposed method with the three implemented baselines across the tested events and operating conditions. The displayed F1-scores are 78.5% for TTM, 84.2% for MA, 91.3% for PG, and 96.8% for the proposed method. The displayed model-side judgment times are 120, 95, 45, and 38 ms, respectively.

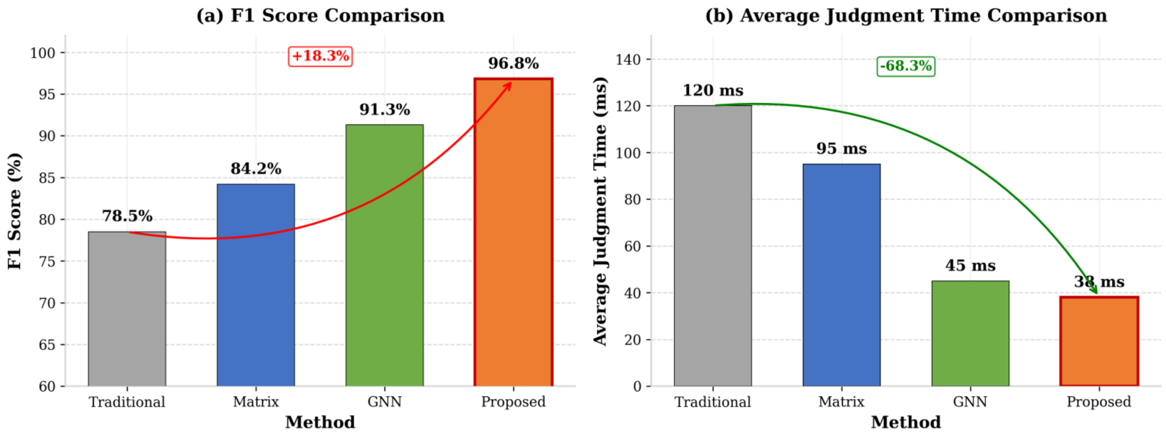

Figure 5. Performance comparison of different outage-identification methods

Table 5 reports a precision of 97.2%, a recall of 96.4%, and an F1-score of 96.8% for the full model. The improved D–S fusion reduces false positives by lowering the contribution of high-entropy evidence instead of applying the same hard rule to every source. The LSTM contributes to early temporal risk assessment by detecting the temporal development of a fault before its instantaneous signature becomes pronounced. The full model requires 38 ms for the measured model-inference-and-fusion stage, whereas removing the improved D–S fusion reduces the measured time to 28 ms but decreases the F1-score to 93.8%. When one channel is corrupted, the remaining independent sources still contribute evidence, and the conflict-dependent D–S weights reduce the influence of the contaminated channel.

Table 5. Ablation study results: contribution analysis of each module

Configuration	Precision (%)	Recall (%)	F1 (%)	F1 Change (%)	Time (ms)
Full Model (Proposed Method)	97.2	96.4	96.8	—	38
Removing LSTM Temporal Module	93.5	91.2	92.3	−4.5	32
Removing GAT Spatial Module	91.8	90.5	91.1	−5.7	35
Removing Improved D–S Fusion	94.6	93.1	93.8	−3.0	28
Removing Supplementary Evidence Mechanism	95.3	94.2	94.7	−2.1	34
Removing Attention Mechanism (GCN replacing GAT)	93.8	92.5	93.1	−3.7	36
Removing DG Impact Compensation	89.4	87.6	88.5	−8.3	38

Removing the DG-impact compensation module reduces the F1-score from 96.8% to 88.5%, corresponding to a decrease of 8.3 percentage points. Without this module, the diagnostic features retain the systematic bias caused by IIDG current limiting, LVRT reactive-current injection, and reverse power flow. Consequently, the same network fault may produce substantially different measured current magnitudes under different DG penetration levels. The compensation module explicitly represents or removes this operating-condition-dependent bias before evidence fusion, allowing the diagnosis model to focus on fault-related residual features. This explains why removing this module causes the largest F1-score degradation among the ablation cases.

Table 6. Diagnostic F1 scores (%) under different signal-to-noise ratio conditions (Scheme C)

Method	40 dB	35 dB	30 dB	25 dB	20 dB	15 dB	10 dB	Average
TTM	80.2	78.5	78.5	78.5	78.5	78.5	78.5	78.8
MA	85.6	84.2	83.1	81.5	79.8	77.2	74.5	80.8
PG	92.5	91.8	90.2	87.4	83.6	78.2	71.5	84.7
Proposed Method	**97.5**	**97.1**	**96.8**	**95.8**	**94.2**	**91.5**	**86.3**	**94.2**

Table 6 reports the F1-scores under different signal-to-noise ratio conditions for Scheme C. The proposed method decreases from 97.5% at 40 dB to 86.3% at 10 dB, whereas MA decreases from 85.6% to 74.5% and PG decreases from 92.5% to 71.5%. TTM changes only from 80.2% to 78.5% because its decision variables do not use the noisy measurement channels. Therefore, the nearly constant TTM values do not demonstrate intrinsic noise robustness. Using (39), the anti-noise scores are 97.9%, 93.5%, 90.6%, and 96.0% for TTM, MA, PG, and the proposed method, respectively. These results are specific to Scheme C and the tested SNR settings.

6. Conclusion

This paper developed a mechanism–data dual-driven outage-identification framework for active distribution networks with high renewable penetration. The framework represents converter-specific fault behavior through a physical feature model and combines this evidence with temporal and graph-based predictions using adaptive D–S weighting. Under the tested feeder, DG operating schemes, fault cases, and measurement-noise conditions, the proposed method achieved an F1-score of 96.8%; its measured model-inference-and-fusion latency was 38 ms, compared with 120 ms for the reference implementation. This measurement excludes data acquisition, communication, timestamp synchronization, and field-device actuation and should not be interpreted as an end-to-end deployment time. The proposed method also achieved higher outage-identification performance than the implemented comparison methods under the tested conditions. These results support the effectiveness of the proposed mechanism–data integration for the studied high-penetration IBDG scenario, but they do not establish universal superiority over all existing methods or distribution-network conditions. The decision chain links early risk assessment, fault diagnosis, and restoration support while retaining interpretable intermediate evidence.

Further work should first test whether reinforcement learning can update the fusion weights online without destabilizing decisions under extreme DG penetration. A second task is to coordinate the different diagnostic horizons: millisecond transient analysis, second-level steady-state assessment, and minute-level outage prediction. The framework can also be connected to an active-distribution-network digital twin so that simulated states and measurements are compared continuously for predictive maintenance. Finally, attention-based feature visualization and physics-informed neural networks that impose the power-system differential–algebraic equations as soft constraints should be evaluated for both accuracy and operator interpretability.

Acknowledgements

This work was supported by the 2025 Science and Technology Project of State Grid Tianjin Electric Power Company, entitled "Research and Application of Mechanism–Data Dual-Driven Technologies for Distribution-Network Outage Identification and Prediction" (Project No. EPRI-S&T-Project-2025-06).

References

[1] Saxena V, Manna S, Rajput SK, et al. Navigating the complexities of distributed generation: integration, challenges, and solutions. Energy Rep. 2024;12:3302-3322.

[2] Majeed AA, Altaie AS, Abderrahim M, et al. A review of protection schemes for electrical distribution networks with green distributed generation. Energies. 2023;16(22):7587.

[3] Tang L, Han Y, Zalhaf AS, et al. Resilience enhancement of active distribution networks under extreme disaster scenarios: a comprehensive overview of fault location strategies. Renew Sustain Energy Rev. 2024;189:113898.

[4] Liao Y, Weng Y, Tan CW, et al. Quick line outage identification in urban distribution grids via smart meters. CSEE J Power Energy Syst. 2022;8(4):1074-1086.

[5] Ibrahim AHM, Sadanandan SK, Ghaoud T, et al. Incipient fault detection in power distribution networks: review,

analysis, challenges, and future directions. IEEE Access. 2024;12:112822-112838.

[6] Nsaif YM, Lipu MSH, Ayob A, et al. Fault detection and protection schemes for distributed generation integrated to distribution network: challenges and suggestions. IEEE Access. 2021;9:142693-142717.

[7] Nguyen BLH, Vu TV, Nguyen TT, et al. Spatial-temporal recurrent graph neural networks for fault diagnostics in power distribution systems. IEEE Access. 2023;11:46039-46050.

[8] Liang L, Zhang H, Cao S, et al. Fault location method for distribution networks based on multi-head graph attention networks. Front Energy Res. 2024;12:1395737.

[9] Lu T, Hou S. Fault location algorithm for distribution network with distributed generation based on domain-adaptive TGATv2. IET Gener Transm Distrib. 2025;19(1):e70033.

[10] Ma X, Zhen W, Ren H, et al. A method for fault localization in distribution networks with high proportions of distributed generation based on graph convolutional networks. Energies. 2024;17(22):5758.

[11] Ma W, Jiang Y, Luo X. A flexible rule for evidential combination in Dempster–Shafer theory of evidence. Appl Soft Comput. 2019;85:105512.

[12] Huang B, Wang J. Applications of physics-informed neural networks in power systems-a review. IEEE Trans Power Syst. 2023;38(1):572-588.

[13] Raissi M, Perdikaris P, Karniadakis GE. Physics-informed neural networks: a deep learning framework for solving forward and inverse problems involving nonlinear partial differential equations. J Comput Phys. 2019;378:686-707.

[14] Zhou Y, Lin H, Liu L, et al. Robust fault location in distribution networks under noisy and incomplete measurements using physics-aware decoupled inference. Energies. 2026;19(11):2583.

[15] Arif A, Wang Z, Wang J, et al. Power distribution system outage management with co-optimization of repairs, reconfiguration, and DG dispatch. IEEE Trans Smart Grid. 2018;9(5):4109-4118.

[16] Malek AF, Mokhlis H, Mansor NN, et al. Power distribution system outage management using improved resilience metrics for smart grid applications. Energies. 2023;16(9):3953.

[17] Jacob RA, Paul S, Chowdhury S, et al. Real-time outage management in active distribution networks using reinforcement learning over graphs. Nat Commun. 2024;15:4766.

[18] Haddadi A, Zhao M, Kocar I, et al. Impact of inverter-based resources on negative sequence quantities-based protection elements. IEEE Trans Power Deliv. 2021;36(1):289-298.

[19] Kim I. A calculation method for the short-circuit current contribution of current-control inverter-based distributed generation sources at balanced conditions. Electr Power Syst Res. 2021;190:106839.

[20] "IEEE Standard for Interconnection and Interoperability of Distributed Energy Resources with Associated Electric Power Systems Interfaces," in IEEE Std 1547-2018 (Revision of IEEE Std 1547-2003) , vol., no., pp.1-138, 6 April 2018, doi: 10.1109/IEEESTD.2018.8332112.

[21] Hochreiter S, Schmidhuber J. Long short-term memory. Neural Comput. 1997;9(8):1735-1780.

[22] Kipf TN, Welling M. Semi-supervised classification with graph convolutional networks. In: Proceedings of the 5th International Conference on Learning Representations (ICLR); 2017; Toulon, France.

[23] Veličković P, Cucurull G, Casanova A, et al. Graph attention networks. In: Proceedings of the 6th International Conference on Learning Representations (ICLR); 2018; Vancouver, BC, Canada.

[24] Tang Y, Zhang X, Zhou Y, et al. A new correlation belief function in Dempster-Shafer evidence theory and its application in classification. Sci Rep. 2023;13:7609.

[25] Rajora GL, Sanz-Bobi MA, Tjernberg LB, et al. A review of asset management using artificial intelligence-based machine learning models: applications for the electric power and energy system. IET Gener Transm Distrib. 2024;18(12):2155-2170.